Bifurcations of rotating waves in rotating spherical shell convection

F. Feudel,[1] L. S. Tuckerman,[2] M. Gellert,[3] and N. Seehafer[1]

[1]*Institut für Physik und Astronomie, Universität Potsdam, Karl-Liebknecht-Strasse 24/25, 14476 Potsdam, Germany*
[2]*PMMH (UMR 7636 CNRS-ESPCI-UPMC Paris 6-UPD Paris 7), 10 rue Vauquelin, 75005 Paris, France*
[3]*Leibniz-Institut für Astrophysik Potsdam, An der Sternwarte 16, 14482 Potsdam, Germany*

The dynamics and bifurcations of convective waves in rotating and buoyancy-driven spherical Rayleigh-Bénard convection are investigated numerically. The solution branches that arise as rotating waves (RWs) are traced by means of path-following methods, by varying the Rayleigh number as a control parameter for different rotation rates. The dependence of the azimuthal drift frequency of the RWs on the Ekman and Rayleigh numbers is determined and discussed. The influence of the rotation rate on the generation and stability of secondary branches is demonstrated. Multistability is typical in the parameter range considered.

PACS number(s): 47.55.P−, 47.32.Ef, 47.20.Ky, 47.54.−r

I. INTRODUCTION

Convection in a spherical shell of viscous fluid heated from the inner sphere and driven by a radially directed volume force represents an idealized model for the large-scale flows in the outer cores of terrestrial planets and in the convection zone of the sun and has for this reason been investigated extensively over the past decades. The pioneering theoretical work of Chandrasekhar [1], Roberts [2], and Busse [3] concentrated primarily on linear stability analyses and asymptotic solutions. Subsequently, as three-dimensional computations became possible, focus shifted to the patterns of finite-amplitude convection and large-scale flows [4–8]. Rotating spherical shell convection is thought to contain the basic ingredients for explaining generic features of geophysical and astrophysical flow dynamics. In particular, if the fluid is electrically conducting, its motion can maintain magnetic fields [9].

In this work, classical Rayleigh-Bénard convection in a rotating shell is revisited by studying multistability of coexisting solution branches, their bifurcations, and their patterns, which appear in the form of rotating waves (RWs). These are also known as thermal Rossby waves. In the asymptotic regime of fast rotation the dispersion relation expected for Rossby waves in the presence of thermal buoyancy is approached [3,10–14].

In a companion investigation [15], we studied this configuration for a fixed rotation rate (corresponding to an Ekman number of 10^{-3}). We found four branches of drifting columnar vortices, each with a different azimuthal wave number. We determined the wave speed along each of these branches, which we found to be a decreasing function of Rayleigh number. We now wish to investigate these trends by varying both the rotation rate and the Rayleigh number.

Takehiro [16] and Kimura *et al.* [17,18] investigated RWs in spherical shells under slightly different conditions. We begin by obtaining similar results, thus confirming their studies. We extend the investigation by not only tracing RWs that bifurcate stably from the conductive state, but also RWs that originate at higher Rayleigh numbers and are therefore unstable at onset. By determining their stability region and computing secondary branches, we try to characterize the multistability of all coexisting solutions in the considered range of control parameters. A similar approach was also used by Sánchez *et al.* [19], but for higher rotation rates and smaller Prandtl

numbers compared to our values of these parameters. The present work is an extension of the studies of Takehiro [16], Kimura *et al.* [17,18], and Sánchez *et al.* [19], which yields a detailed description of the coexisting solution branches and their bifurcations.

A. Governing equations

We study buoyancy-driven Rayleigh-Bénard convection in a spherical shell rotating with a constant angular velocity $\boldsymbol{\Omega} = \Omega \boldsymbol{e}_z$ about the z axis and heated from within imposing a temperature difference ΔT between its spherical boundaries. Using the gap size d as the unit length scale, scaling time by the viscous time d^2/ν (where ν is the kinematic viscosity), and temperature by ΔT, the equations in Boussinesq approximation can be written in nondimensional form as

$$\mathrm{Ek}\left[\frac{\partial \boldsymbol{u}}{\partial t} + \boldsymbol{u} \cdot \nabla \boldsymbol{u} - \nabla^2 \boldsymbol{u}\right] = -\nabla P + \mathrm{Ra}\, T \frac{\boldsymbol{r}}{r_0} - 2\boldsymbol{e}_z \times \boldsymbol{u}, \tag{1a}$$

$$\frac{\partial T}{\partial t} + \boldsymbol{u} \cdot \nabla T = \frac{1}{\mathrm{Pr}}\nabla^2 T, \tag{1b}$$

$$\nabla \cdot \boldsymbol{u} = 0, \tag{1c}$$

where

$$\mathrm{Ek} = \frac{\nu}{d^2 \Omega}, \quad \mathrm{Ra} = \frac{\alpha\, \Delta T\, g_0\, d}{\Omega \nu}, \quad \mathrm{Pr} = \frac{\nu}{\kappa}$$

are the Ekman number, a modified Rayleigh number (α is the thermal expansion coefficient and g_0 is the magnitude of the gravitational acceleration at the outer radius), and the Prandtl number (κ is the thermal diffusivity), respectively. In Eq. (1a), the centrifugal acceleration and a gradient part of acceleration due to buoyancy have been incorporated into P.

Our modified Rayleigh number is related to the conventional Rayleigh number $\widetilde{\mathrm{Ra}}$ via $\mathrm{Ra} = \widetilde{\mathrm{Ra}}\,\mathrm{Ek}/\mathrm{Pr}$. Normalizations of this kind are often used in dynamo studies [20–22]. A discussion of different definitions of the Rayleigh number in the context of geodynamo simulation was given by Kono and Roberts [23]. The fourth and last nondimensional parameter specifies the geometry and can be given by either

the nondimensional outer radius, r_o, or, equivalently, the radius ratio $\eta = r_i/r_o = (r_o - 1)/r_o$.

Following a dynamo benchmark study [22] and a preceding work [15] we fix the Prandtl number to Pr = 1 and the radius ratio to $\eta = 0.35$, i.e., the dimensionless radii $r_o = 20/13$ and $r_i = 7/13$. This value of η is estimated to be close to that of the outer core of the Earth. In contrast, the Prandtl number Pr = 1 does not correspond to realistic geophysical applications. However, from Ref. [22] it is known that self-sustained dynamos exist for these parameters, and we have chosen them in order to prepare for a future investigation on dynamo bifurcations in an electrically conducting fluid. The Ekman number Ek and the Rayleigh number Ra are varied in this study.

The spherical boundaries are assumed to be rigid and perfectly conducting:

$$\boldsymbol{u} = 0 \text{ at } r = r_i, r_o, \tag{2a}$$

$$T = 1 \text{ at } r = r_i \quad \text{and} \quad T = 0 \text{ at } r = r_o. \tag{2b}$$

B. Numerical approach

A spectral time-stepping code developed by Hollerbach [24] constitutes the basic ingredient of a path-following method implemented for tracing the RWs. We summarize its features here; more details can be found in Ref. [15]. The spatial discretization in (r, θ, φ) uses an expansion in complex spherical harmonics of 36 wave numbers both in latitudinal and longitudinal directions, and in Chebyshev polynomials up to a degree of 36.

Equations (1) and (2) can be represented schematically in the form

$$\frac{\partial \boldsymbol{U}}{\partial t} = L(\boldsymbol{U}) + N(\boldsymbol{U}), \tag{3}$$

where $\boldsymbol{U}$ is the state vector, $L(\boldsymbol{U})$ a linear operator, whose time-integration is treated implicitly, and $N(\boldsymbol{U})$ contains the terms which are treated explicitly.

In spherical polar coordinates RWs are characterized by the condition $\boldsymbol{U}(r, \theta, \varphi) = \boldsymbol{U}(r, \theta, \varphi_0 - \omega t)$, where ω is the angular velocity of the RW (also referred to as drift frequency). Equation (3) reduces to a fixed point problem of the form

$$0 = L(\boldsymbol{U}) + N(\boldsymbol{U}) - \omega \boldsymbol{U}, \tag{4}$$

which is solved by a matrix-free Newton iteration. As described by Mamun and Tuckerman [25], the implicit integration of L plays the role of a preconditioner in solving the resulting linear system, which is solved by either the generalized minimal residual method (GMRES) [26] or the biconjugate gradient stabilized method (BICGSTAB) [27]. The convergence of these two methods is comparable and is greatly deteriorated by the antisymmetric contribution of the Coriolis term for higher rotation rates.
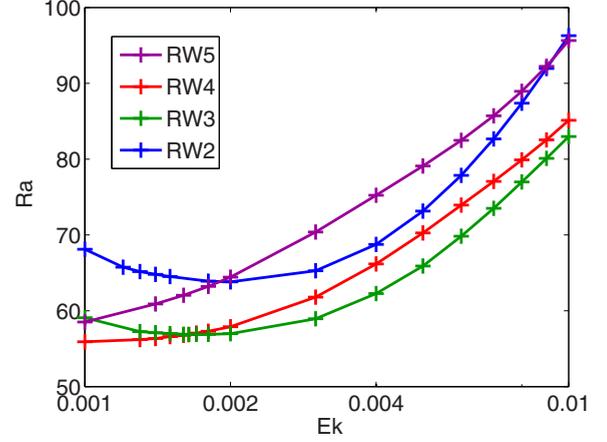
FIG. 1. (Color online) Critical Rayleigh numbers of the $m = 2, 3, 4, 5$ modes as a function of the Ekman number plotted with a logarithmic scale for Ek. Crosses label the points at which bifurcations have been calculated; the solid lines are drawn to guide the eye.

II. PRIMARY BIFURCATIONS

The basic conductive state, with the fluid at rest and the temperature profile given by

$$T_c(r) = \frac{r_o(r_o - 1)}{r} - r_o + 1, \tag{5}$$

is stable for low Rayleigh numbers at all Ekman numbers. For moderate rotation rates $0.001 \leqslant \text{Ek} \leqslant 0.01$ the basic state loses stability in a supercritical Hopf bifurcation. Figure 1 depicts the Rayleigh numbers at which modes with azimuthal wave numbers $m = 2, 3, 4, 5$ acquire positive growth rates and rotating waves (RWs), in the following denoted by RW2, RW3, RW4, and RW5, bifurcate from the conductive state. For the linear stability analysis of Fig. 1, the computation is restricted to a single value of m. The resulting eigenmodes serve subsequently as initial conditions for the path-following procedure. States on a given branch contain a primary azimuthal wave number and its harmonics, i.e., multiples of the main wave number, including the $m = 0$ component, which is the mean flow.

The azimuthal wave numbers of the RWs and the order in which they bifurcate is determined primarily by the geometry, i.e., in this case the radius ratio. Systems such as Rayleigh-Bénard convection or Taylor-Couette flow favor rolls whose cross-sections are nearly equal in both directions. Setting the azimuthal cross-sections $\frac{\pi(r_o + r_i)}{2m}$ of a roll equal to the radial cross-section $r_o - r_i$ leads to

$$\frac{\pi}{2m} = \frac{r_o - r_i}{r_o + r_i} = \frac{1 - \eta}{1 + \eta},$$

which yields $m = 3.26$ for the value of η considered in this study. The preferred wave number is about 3 and bifurcations to RWs with wave numbers that are farther from 3, i.e., $m = 1$ or $m > 5$ would occur at higher values of Ra.

The succession and the Rayleigh numbers at which the RWs appear also depend on the Ekman number. For Ek ≈ 0.001, cf. Fig. 1, the RW5 and RW3 solutions are the second and third to bifurcate, while for slightly higher Ekman numbers they
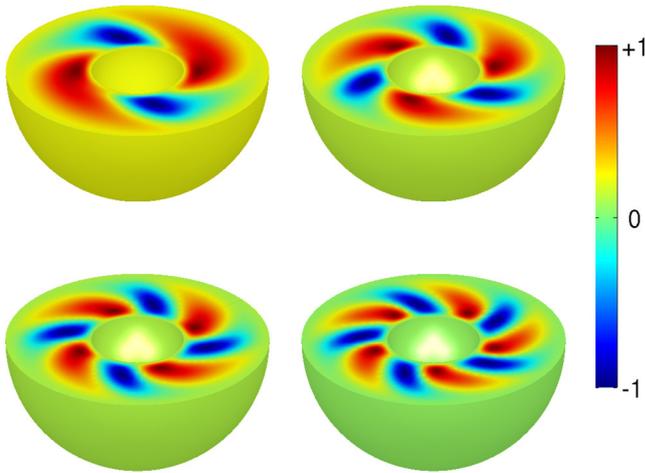
FIG. 2. (Color online) Radial velocity normalized to its maximum modulus in the equatorial plane for RW2 (top left), RW3 (top right), RW4 (bottom left), and RW5 (bottom right) at Ek = 0.001 and Ra = 100. Positive values (red) correspond to radial outflow and negative values (blue) to radial inflow.
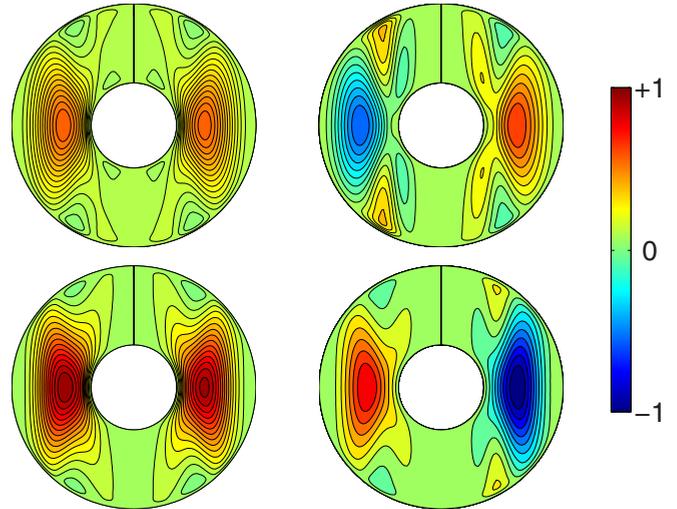
FIG. 3. (Color online) Radial velocity in the meridional plane at Ek = 0.001 and Ra = 100. RW2 (top left), RW3 (top right), RW4 (bottom left), and RW5 (bottom right).

exchange their bifurcation order. The value of Ek = 0.001 was the subject of our previous study [15]; in this sequel, we extend the investigation to the interval $0.001 \leqslant$ Ek $\leqslant 0.01$, focusing on the qualitative effect of the rotation rate on the solution branches.

Equations (1) and (2) are equivariant with respect to the symmetry group $SO(2) \times Z_2$, where the special orthogonal group $SO(2)$ consists of rotations about the z axis and the Z_2 group is generated by reflection in the equatorial plane. Under these circumstances, Hopf bifurcations that break the azimuthal symmetry generate patterns of RWs drifting rigidly along the azimuthal direction [28–30]. The equatorial reflection symmetry is retained and the bifurcating RWs exhibit a cyclic symmetry Z_m determined by the critical mode number m. The critical Rayleigh numbers shown in Fig. 1 were calculated for a discrete set of Ekman numbers. For these Ekman numbers, the bifurcating RW branches were traced systematically by varying the Rayleigh number.

The RWs are visualized by contour plots of the radial velocity in the equatorial plane. In Fig. 2 these patterns are presented for Ek = 0.001 and Ra = 100, at which four RW solutions coexist. The flow pattern consists of m counterrotating vortex pairs around the inner boundary, sometimes referred to as Busse columns. In accordance with the Taylor-Proudman theorem, the rolls become increasingly straight and parallel to the rotation axis as the Ekman number is decreased, while they curve around the inner sphere for smaller rotation rates. The cross-sectional areas of the convection rolls spiral outwards in the prograde direction. Figure 3 presents views of the RWs in a meridional plane. The plane shown is rotated by $\pi/6$ counterclockwise about the z axis with respect to the meridional plane that would be seen in front view in the perspective of Fig. 2.

We now study the RW branches, in particular their stability and secondary bifurcations over the Ekman number interval $0.002 \leqslant$ Ek $\leqslant 0.01$. As seen in Fig. 1, in this interval the $m = 3$ mode is the first to become unstable when Ra is

increased, followed by the $m = 4$, $m = 2$, and $m = 5$ modes. The bifurcation diagrams of the corresponding RWs branches are drawn separately in Figs. 4–7. The solution branches were computed, first, for a discrete set of Ekman numbers while varying the Rayleigh number, and second, for two fixed Rayleigh numbers, Ra = 80 and Ra = 100, while varying the Ekman number. The kinetic energy $\int |\boldsymbol{u}|^2 dV$ integrated over the spherical shell serves as a convenient order parameter in these three-dimensional bifurcation diagrams. Stable parts of the branches are drawn as thick lines and unstable parts as thin lines. It can immediately be seen that the RW3 solutions, cf. Fig. 4, resulting from the critical mode are dominant in the sense that they are stable over a wide range of the Ekman-Rayleigh number control parameter plane. However, the RW4 (Fig. 5), RW2 (Fig. 6), and RW5 (Fig. 7) branches are also stabilized in secondary bifurcations, leading to multistability.
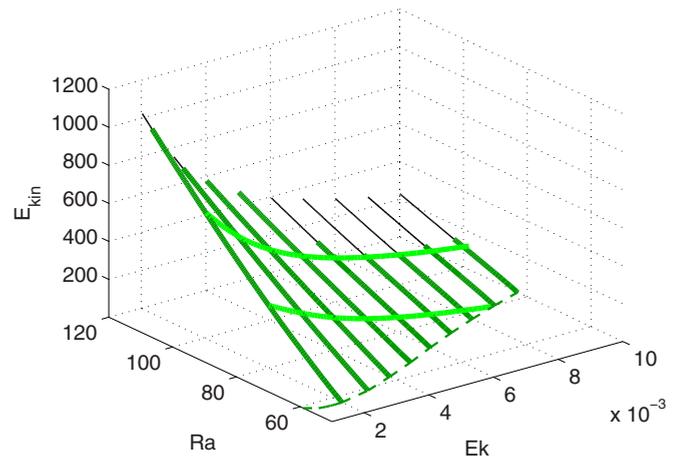
FIG. 4. (Color online) Kinetic energy of RW3 as function of the Ekman and Rayleigh numbers. Thin (thick) lines correspond to unstable (stable) solutions and the lower dashed line shows the critical Rayleigh number as function of the Ekman number.

FIG. 5. (Color online) Same as described in the caption of Fig. 4, but for RW4.
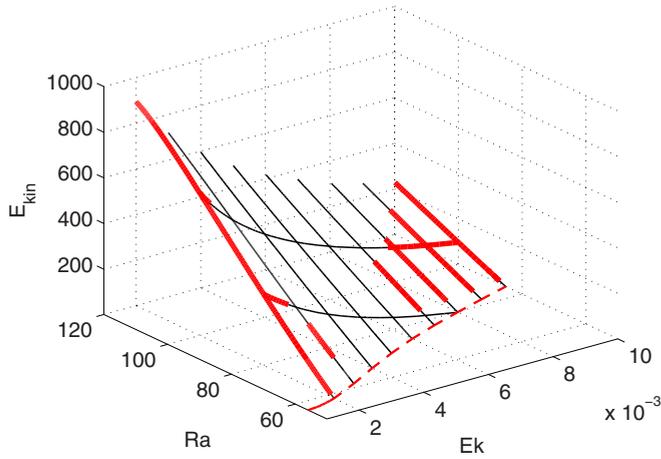
FIG. 7. (Color online) Same as described in the caption of Fig. 4, but for RW5.

In particular, for Ek = 0.001 and Ra = 100, the parameter values of Fig. 2, all four RWs are stable.

We note that for certain values of the Ekman numbers, $0.004 \leqslant \text{Ek} \leqslant 0.006$, the RW4 solutions all remain unstable, cf. Fig. 5, but for higher values, approximately $\text{Ek} \geqslant 0.0065$, this branch is stabilized. The RW5 solutions exhibit similar stability behavior, cf. Fig. 7. They are also stabilized for larger Ekman numbers, remain unstable for smaller ones, and become stable again for high rotation rates, $\text{Ek} \approx 0.001$, not shown in Fig. 7 but discussed in Ref. [15].

Figure 8 shows the Nusselt-number dependence of the rotating waves for various m and Ek values, with stable and unstable portions highlighted, as in Figs. 4–7. To summarize, over our parameter ranges, the $m = 3$ branches are stable over a large range of Ra for all Ek studied, the $m = 4$ branches are created unstable but restabilize at higher Ra for low and high values of Ek, but not for intermediate values, and the $m = 2$ ($m = 5$) branches restabilize only for low (high) Ek.

The physical mechanisms underlying the RW propagation or drift have been a focus of investigation of rotating spherical shell convection [5,15–18]. In particular the question under
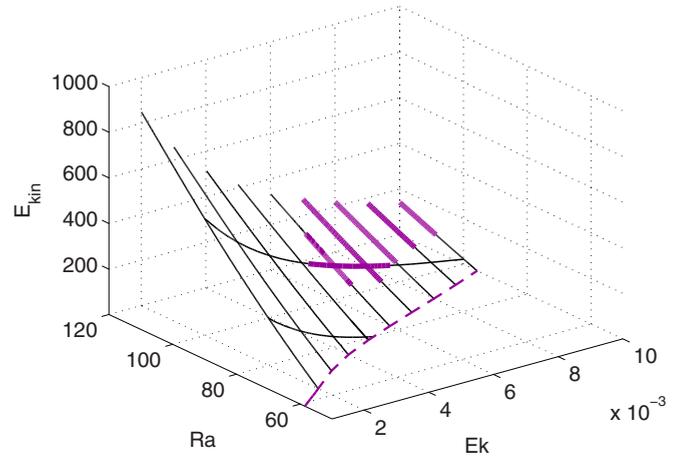
which conditions the drift is prograde or retrograde with respect to the rotating frame and how the drift direction and rate depend on the Ekman and Rayleigh numbers is still under discussion in the literature.

In Ref. [15] we studied reversals of the RW drift direction for Ek = 0.001. Here, as in the preceding part of this section, we extend the investigation to a wider range of the control parameters. Figure 9 presents the dependence of the drift frequency ω on the Rayleigh number for the RWs at the Ekman numbers 0.008, 0.006, 0.004, and 0.002. Positive (negative) values of ω correspond to prograde (retrograde) propagation. Two features are seen:

(i) At the critical Rayleigh numbers, where the convection sets in, the propagation direction is retrograde for small rotation rates (large Ekman numbers) and changes to prograde for large rotation rates (small Ekman numbers). In particular, for the smallest Ekman number, Ek = 0.002 (right bottom

FIG. 6. (Color online) Same as described in the caption of Fig. 4, but for RW2.
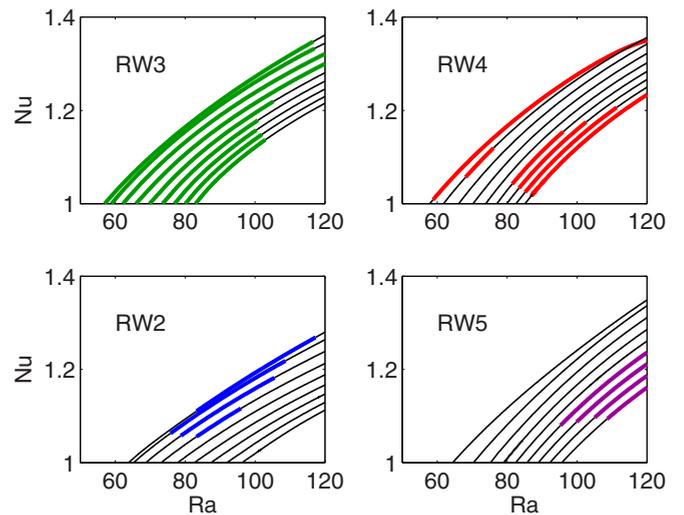
FIG. 8. (Color online) Nusselt-number dependence of the rotating waves. For each m, curves from left to right correspond to Ek = 0.002, 0.003, 0.004, 0.005, 0.006, 0.007, 0.008, 0.009, 0.01.
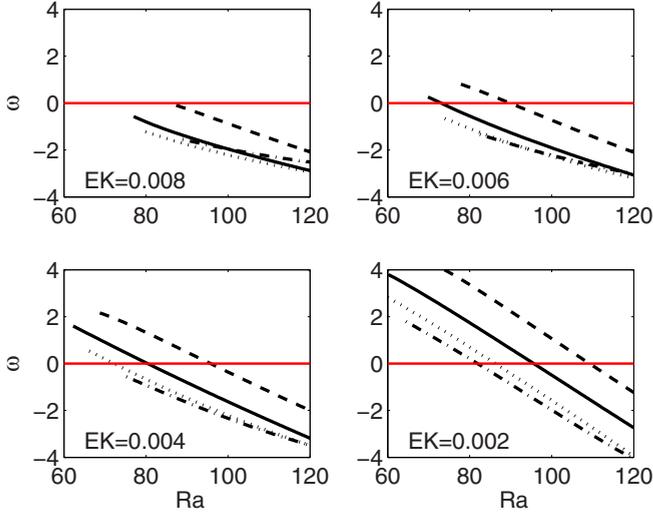
FIG. 9. (Color online) Drift frequency ω as function of Ra for RW2 (dashed line), RW3 (solid line), RW4 (dotted line), and RW5 (dash-dotted line).

panel), all the RWs considered propagate in the prograde direction at onset.

(ii) For a given branch at a fixed Ekman number, ω decreases continuously as the Rayleigh number is increased. That is, if ω is negative at onset, it remains negative, with increasing modulus as Ra is increased. If, on the other hand, the convection sets in with prograde propagation, the drift frequency decreases with increasing Ra until eventually the propagation reverses from the prograde to the retrograde direction.

From the observations (i) and (ii) we may draw two conclusions:

(a) The convective motions generate a retrograde drift. The stronger these motions, the stronger the generated drift.

(b) The drift at the onset of convection originates by a mechanism different from that responsible for the drift described in (a) since it sets in at a finite rate when the motions are vanishingly weak.

So there are, seemingly, two different drift-generation mechanisms at work. This agrees with a similar conclusion of Kimura *et al.* [17]. These authors attribute the retrograde-prograde transition for increasing rotation rate at the convection onset to the changing shape and location of the convective vortices (curved around the inner sphere for small rotation rates and increasingly straight and parallel to the rotation axis as the rotation rate is increased). In contrast, they attribute the reversal of the drift direction at fixed rotation rate for increasing Rayleigh number along a given branch to the mean zonal flow.

The importance of angular momentum conservation and transport arises from the fact that, at least in the limit of fast rotation, the RWs can be interpreted as Rossby waves, the underlying physical principle of which is angular momentum conservation or, equivalently, potential vorticity conservation. In our investigations we observed a correlation between angular momentum transport and the RW drift [31]. For all branches at fixed Ekman number, prograde axial angular momentum ($L_z > 0$) is transported through the spherical

shell, into the shell at the inner boundary and at the same rate out of the shell at the outer boundary, beginning from zero at the convection onset and increasing with increasing Rayleigh number. In order to explain this effect a more detailed investigation will be necessary.

III. SECONDARY BIFURCATIONS

While we have discussed the stability of the RWs in Sec. II, in particular the points at which the RWs acquire or lose stability, we have not yet discussed the type of secondary bifurcations that are responsible. In many cases the RWs undergo subcritical Hopf bifurcations engendering unstable modulated rotating waves (MRWs), which cannot be calculated by time-dependent simulations, while the tracing of unstable MRW branches by path-following methods is a numerical task that goes beyond this study.

We therefore cannot elucidate all secondary bifurcations. Instead, we will discuss a specific example, in which the RW4 branch undergoes a symmetry-breaking bifurcation reducing the Z_4 symmetry to Z_2, corresponding to rotation by π about the z axis. We denote the state that is created by this bifurcation as RW4-2 to indicate that the state has an $m = 2$ component as well as the multiples of $m = 4$ contained by RW4.

In order to demonstrate how this bifurcation evolves with the rotation rate, in Fig. 10 the RW4 and the bifurcating RW4-2 branches are shown for three selected values of the Ekman number, namely 0.003, 0.004, and 0.007. At Ek = 0.003, the top panel in Fig. 10, the RW4 branch is stable for $68.2 < \text{Ra} < 76.1$ and loses stability in a Hopf bifurcation at the upper end of this interval, at which stable MRWs (not depicted here) are born. For a higher Ra along the now unstable RW4 branch a further subcritical symmetry-breaking pitchfork bifurcation occurs, creating the highly unstable RW4-2 states, which have a rotational Z_2 symmetry.
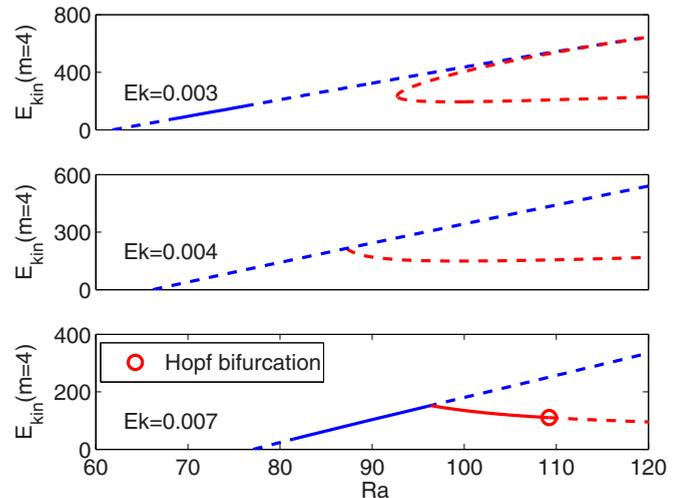
FIG. 10. (Color online) Bifurcations breaking the Z_4 symmetry of the RW4 branch and generating a new branch, RW4-2, with Z_2 symmetry are drawn in the plane spanned by Ra (abscissa) and the kinetic energy contained in the $m = 4$ mode (ordinate). The RW4 (RW4-2) branches are shown in blue (red). From top to bottom, Ek = 0.003, Ek = 0.004, and Ek = 0.007. Solid (dashed) lines mark the stable (unstable) parts of the RWs.
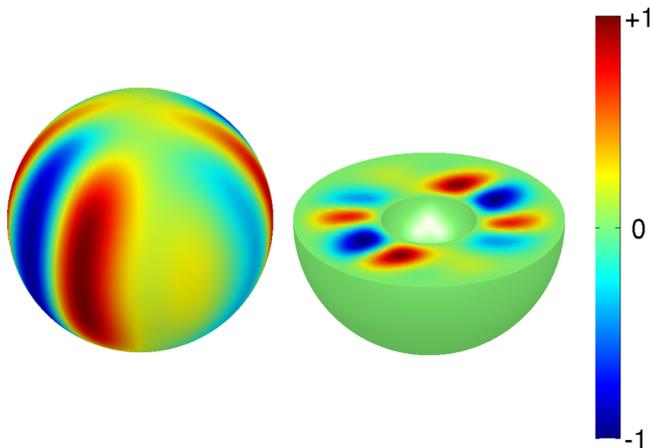
FIG. 11. (Color online) Radial velocity as in Fig. 2, but for the RW4-2 solution at Ek = 0.007 and Ra = 120 at midgap (left) and in the equatorial plane (right).

As the Ekman number is increased, the RW4 branch becomes unstable over our entire Rayleigh-number range, cf. middle panel in Fig. 10 for Ek = 0.004. Eventually the RW4 branch is restabilized by other secondary bifurcations in this scenario, as depicted for Ek = 0.007 in the bottom panel. There now exists a stable part of the RW4 branch from which the stable RW4-2 solutions branch off, now in a supercritical bifurcation.

The RW4-2 branch loses stability in a further Hopf bifurcation at Ra = 109.2, cf. bottom panel of Fig. 10. Generically MRWs must originate at this bifurcation, and indeed, we have observed MRWs just above the Hopf threshold. We have observed that beyond this point, the solution jumps to another branch where two other frequencies appear in addition to the drift frequency, indicating a transition to a nongeneric three-torus branch for which all modes become excited. The further transitions to chaos are beyond the scope of this study.

The RW4-2 solution is illustrated in Fig. 11, where contour plots of the radial velocity in the middle of the spherical gap (left) and in the equatorial plane (right) are shown at Ek = 0.007. Since the contribution of the $m = 2$ mode is rather weak on the stable part of the RW4-2 branch we have chosen a larger value for the Rayleigh number, namely Ra = 120, to make this effect visible.

IV. CONCLUSIONS

In this work we computed systematically the RWs for different dominant azimuthal wave numbers m, studied their stability, and described secondary bifurcations. It is demonstrated that by the use of path-following techniques and the computation of unstable as well as stable branches a deeper understanding of the qualitative solution behavior can be acquired than is possible by pure time-dependent simulations. In particular, this approach yields an extensive exposition of the coexisting solutions and their multistability.

In a future study, we extend this approach to the magneto-hydrodynamic equations by adding the induction equation and the Lorentz force in order to reveal the origin of the dynamo effect.

[1] S. Chandrasekhar, *Hydrodynamic and Hydromagnetic Stability* (Oxford University Press, New York, 1961).

[2] P. H. Roberts, Philos. Trans. R. Soc. London A **263**, 93 (1968).

[3] F. H. Busse, J. Fluid Mech. **44**, 441 (1970).

[4] G. Geiger and F. H. Busse, Geophys. Astrophys. Fluid Dynam. **18**, 147 (1981).

[5] K.-K. Zhang and F. H. Busse, Geophys. Astrophys. Fluid Dynam. **39**, 119 (1987).

[6] M. Ardes, F. H. Busse, and J. Wicht, Phys. Earth Planet. Inter. **99**, 55 (1997).

[7] A. Tilgner and F. H. Busse, J. Fluid Mech. **332**, 359 (1997).

[8] R. Simitev and F. H. Busse, New J. Phys. **5**, 97 (2003).

[9] F. H. Busse, Phys. Fluids **14**, 1301 (2002).

[10] K. Zhang, Phys. Earth Planet. Inter. **68**, 156 (1991).

[11] K. Zhang, J. Fluid Mech. **236**, 535 (1992).

[12] K. Zhang and C. A. Jones, Geophys. Astrophys. Fluid Dynam. **71**, 145 (1993).

[13] C. A. Jones, A. M. Soward, and A. I. Mussa, J. Fluid Mech. **405**, 157 (2000).

[14] E. Dormy, A. M. Soward, C. A. Jones, D. Jault, and P. Cardin, J. Fluid Mech. **501**, 43 (2004).

[15] F. Feudel, N. Seehafer, L. S. Tuckerman, and M. Gellert, Phys. Rev. E **87**, 023021 (2013).

[16] S.-I. Takehiro, J. Fluid Mech. **659**, 505 (2010).

[17] K. Kimura, S.-I. Takehiro, and M. Yamada, Phys. Fluids **23**, 074101 (2011).

[18] K. Kimura, S.-I. Takehiro, and M. Yamada, Phys. Fluids **25**, 084107 (2013).

[19] J. Sánchez, F. Garcia, and M. Net, Phys. Rev. E **87**, 033014 (2013).

[20] P. Olson and G. A. Glatzmaier, Phys. Earth Planet. Inter. **92**, 109 (1995).

[21] U. Christensen, P. Olson, and G. A. Glatzmaier, Geophys. Res. Lett. **25**, 1565 (1998).

[22] U. Christensen, J. Aubert, P. Cardin, E. Dormy, S. Gibbons, G. Glatzmaier, E. Grote, Y. Honkura, C. Jones, M. Kono *et al.*, Phys. Earth Planet. Inter. **128**, 25 (2001).

[23] M. Kono and P. H. Roberts, Phys. Earth Planet. Inter. **128**, 13 (2001).

[24] R. Hollerbach, Int. J. Num. Meth. Fluids **32**, 773 (2000).

[25] C. K. Mamun and L. S. Tuckerman, Phys. Fluids **7**, 80 (1995).

[26] Y. Saad and M. H. Schultz, SIAM J. Sci. Stat. Comput. **7**, 856 (1986).

[27] H. A. van der Vorst, SIAM J. Sci. Stat. Comput. **13**, 631 (1992).

[28] E. Knobloch, in *Lectures on Solar and Planetary Dynamos*, edited by M. R. E. Proctor and A. D. Gilbert (Cambridge University Press, Cambridge, 1994), pp. 331–372.

[29] P. Chossat and R. Lauterbach, *Methods in Equivariant Bifurcations and Dynamical Systems* (World Scientific, Singapore, 2000).

[30] R. E. Ecke, F. Zhong, and E. Knobloch, Europhys. Lett. **19**, 177 (1992).

[31] S. Müller, Diploma thesis, University of Potsdam (2015).